Semi-analytical thermo-mechanical model for the shield tunnel segmental joint subjected to elevated temperatures

Semi-analytical thermo-mechanical model for the shield tunnel segmental joint subjected to elevated temperatures

Yi Shen [b,c] , He-hua Zhu [a, c], Zhi-guo Yan [a,c,*] ,Long Zhou[b,c], Yong Lu[d]

[a] *State Key Laboratory of Disaster Reduction in Civil Engineering, Tongji University, 1239 Siping Road, Shanghai 200092, China*

[b] *Department of Geotechnical Engineering, Tongji University, 1239 Siping Road, Shanghai 200092, China*

[c] *Key Laboratory of Geotechnical and Underground Engineering of the Ministry of Education, Tongji University, 1239 Siping Road, Shanghai 200092, China*

[d] *Institute for Infrastructure and Environment, School of Engineering, University of Edinburgh, Edinburgh EH9 3JL, UK*

Abstract

The segmental joint is the most critical component for determining the mechanical response of concrete segmental linings in a shield-tunnel structure. Existing segmental joint models have been developed mainly for the analysis of segmental lining design, but in the event of a fire, the conditions that a tunnel joint may experience could well exceed the normal design range. Consequently, the validity of the existing segmental joint models becomes questionable. In this paper, an improved semi-analytical thermo-mechanical model is derived based on the general plane joint model to consider the thermal effect induced by elevated temperatures. As a benchmark for the development of the model, a laboratory experiment was conducted on concrete lining segmental joints under elevated temperatures. The general heat transfer and special heat flow invading through the joint were deduced by theorical and numerical methods. A finite element (FE) model is developed and calibrated against experimental model tests, whilst the FE model is

employed to generate the required parametric data, from which a fitting function is created. A temperature adjustment coefficient is introduced to improve the calculation of the joint section temperature field. The influence of elevated temperature and axial force on the bending moment of a segmental joint is also incorporated according to the stress state of the joint section. The validation of the proposed semi-analytical thermo-mechanical model is demonstrated through comparisons with the results of fire tests. Finally, the influences of the heating curves, bolt location, and axial load on the rotation stiffness of the joint are investigated using the proposed model.

Keywords: shield tunnel; segmental joint; fire; semi-analytical model

1 # Nomenclature

A_b	area of the bolt	$T(t)$	gas temperature inside the furnace
b	width of the segmental joint	$T(x,t)$	temperature of the tunnel lining at depth x and time t
C_1	resultant force of joint-concrete compressive zone	T_f	temperature of thermal flue gas flow in fire
$E_c(x,T)$	elastic modulus of the concrete at the height x under temperature T	T_0	initial temperature of tunnel lining
$E_b(x,T)$	elastic module of the bolt under temperature T	α	thermal diffusivity of the lining concrete
$erfc(u)$	Gauss error complementary function	δ_c	deformation in the outer edge of the compressive zone of joint
F_b	tension force supported by one bolt	ε_a	maximum strain of compression zone under full pressure
H	thickness of the tunnel linings	ε_b	tensile strain of the bolt
h	surface heat transfer coefficient of the tunnel lining	ε_c	strain of edge point of compression zone
h_b	height of bolt	ε_t	minimum strain of compression zone under full pressure
h_c	height of the compressive zone	ζ	temperature adjustment coefficient of the bolt
K_θ	bending resistance stiffness of joint	η	coefficient of concrete at the joint temperature adjustment
l_b	length of the bolt	θ	opening angle of the lining joints
M	bending moment	λ	thermal conductivity of the lining concrete
M_{C1}	bending moment of C_1 to Point ***O***		
N	axial force		
n	number of bolts		

2

3

1 Introduction

Tunnel fires post serious threat to the safety of tunnel users. Cafaro and Bertola (2010) and Vianello et al. (2012) summarized a number of tunnel fires with casualties occurred in Europe during the last decades, for instance the Mont Blanc fire at the France–Italy border in 1999 (39 casualties), Tauern fire in Austria in 1999 (12 casualties) and Gothard fire in Switzerland in 2001 (11 casualties). Because of the characteristics of high peak temperature, rapid heating rate, long duration and nonuniform temperature distribution inside tunnels, tunnel fires have also been associated with severe damages to concrete tunnel linings (Kim et al., 2010; Zhao et al., 2017; Yan et al., 2015; 2020). Concrete segmental linings, which are continuously placed side-by-side as tunnel boring machine (TBM) advances, are commonly used in shield-driven tunnels (Zhu, 1995; Zhong et al, 2006). One of the most important factors in designing a segmental tunnel lining is the influence of segmental joints on structural overall behavior. For the concrete shield TBM tunnel lining in soft ground with high water pressure, fire damages may also lead to seal failure of the lining joints, resulting in tunnel leakage (Yan et al., 2012; 2013; 2016).

The mechanical behavior of the joints under ambient temperature has been the subject of extensive study in the past. Blom (2002) classified bending stiffness of segment joint into three stages: constant stiffness, reduced stiffness and reduced stiffness with plastic stresses. Arnau and Molins (2011) proposed a consistent model of the tunnel behavior through the simulation of the detailed behavior of the joints between lining segments. The development of the opening angle of the joint is recognized to affect

significantly the rotational stiffness of the joint. On the other hand, axial and shear stiffness of segment joints have a negligible effect on segmental lining behavior (Do et al., 2013; Hao et al., 2018). Under large eccentric load, failure occurs when the maximum compressive stress reaches the ultimate value in the compressive zone of the joint (Huang et al., 2016; Zhang and Koizumi, 2007).

A typical approach to modelling the segmental joint is by means of rotational springs located at the joints (Teachavorasinskun and Chub-Uppakarn, 2002; Ding et al., 2004). Such a model has the advantage of easy implementation in a bedded beam model for the tunnel lining structure. The stiffness of the rotational springs is often considered as a constant for simplicity (Lee and Ge, 2001; El Naggar and Hinchberger, 2008). However, the same joint can exhibit different rotational behaviors under different axial stress levels. Therefore, the predicted joint opening may not be accurate if the effect of axial stress levels on the joint behavior is neglected (Li et al., 2015a). Structural tests show that the rotational stiffness is higher when a joint is subjected to a positive bending moment than when it is subjected to a negative bending moment (Li et al., 2015b). Furthermore, the rotational stiffness of a longitudinal joint changes dramatically after the joint is opened as compared to the state when the longitudinal joint is closed. In this respect, a rotational spring with either bilinear (Koyama, 2003; Zhong et al., 2006) or nonlinear (Zhu, 1996) constitutive model has been proposed to describe the relationship between joint rotational angle and bending moment.

Despite these efforts, so far there has been limited study on the mechanical behavior

of segmental joints under elevated temperature due to fire. Yasuda et al. (2004) conducted a full-scale fire test on shield TBM tunnel composite segments under a RABT fire curve for. It was found that spalling of concrete reached up to 60 mm when there was no fire protection on the surface. Caner and Böncü (2009) performed hydrocarbon fire tests on an isolated segment of a shield TBM tunnel to investigate fire damage to the segment concrete. This study concluded that the deviation in safety factor of the TBM tunnel in the hydrocarbon fire as the tunnel became more flexible. Yan et al. (2012) carried out full-scale experiments to investigate fire damage to metro shield TBM tunnel linings tested to a standard ISO834 fire curve. The results indicated that, under the ISO834 curve with duration of 90 min, the maximum temperature of the reinforcement of the tunnel linings could exceed the failure temperature. Considering that the shield TBM tunnel is a statically indeterminate structure assembled by multiple member segments by lining joints, its behavior and failure mechanism under elevated temperature can be complicated (Yan et al., 2012). Among other factors, the behavior of the lining joint under high temperature is a key to the overall performance of the shield TBM tunnel lining in fire. However, little research has been reported on the bending behavior of the shield TBM tunnel lining joints under elevated temperatures (Yan et al., 2013, 2016).

In this paper a semi-analytical thermo-mechanical model is proposed to analyse the bending behavior of the shield tunnel segmental joint exposed to elevated temperatures. Verification against experimental results indicates that this model is suitable for the analysis of the response of shield tunnel segmental joint under elevated temperatures. The

phenomenon of heat flow invading through the joint is discussed and quantified. Finally, potential applications of this model are presented based on holistic parametric study on the influences of heating curves, bolt location and axial load.

2 Benchmark experimental study

As a benchmark for the development of the model, a laboratory experiment was conducted on concrete lining segmental joints under elevated temperature. An overview of the experiment is given in this section. More details of the experimental investigation can be found from Yan et al. (2016). Herein we define that sagging (positive) bending moment produces concave bending at the middle of a simply supported beam, while hogging (negative) bending moment produces raised bending at the middle of a simply supported beam.

2.1 Test specimens

Fig. 1 shows the configuration and details of the test specimens. The test specimens were made of reduced-scale lining segments of 300 mm in width and 120 mm in thickness, and the average radius was 990 mm, and each specimen was an assembly of two segments. The two segments were connected via a joint by two curved steel bolts of 10mm in diameter and yield strength 400 MPa. The main reinforcement of RC lining segment was hot rolled ribbed steel bar of 10 mm in diameter and yield strength 300 MPa, and the stirrups were hot rolled plain bar of 6.5 mm in diameter and yield strength of 235 MPa. The strength of the concrete for the specimen was 60MPa. To represent an actual metro

shield TBM tunnel lining segment, important details such as the hand hole, the longitudinal tongue and groove of the lining segment were represented in the test specimens.

One specimen (RC0) was subjected to loading test, under a constant horizontal force of 40kN, in ambient temperature as a benchmark. Three specimens were subjected to loading tests under fire, including RCJ1 (under a constant horizontal force of 20kN), RCJ2 (under a constant horizontal force of 40kN) and RCJ3 (under a constant horizontal force of 60kN).

2.2 Test set-up

The test was conducted using a thermo-mechanical test system for tunnel lining segments, as shown in **Fig. 2**. In this experiment, the standard European HC curve (CEN, 2005) was employed in the experimental tests to simulate the heating phase:

$$T(t) = 20 + 1080\,(1 - 0.325\mathrm{e}^{-0.167t} - 0.675\mathrm{e}^{-2.5t}) \tag{1}$$

where t is time (in minutes) and $T(t)$ is the gas temperature inside the furnace (in ˚C).

The test segments were heated following the standard European HC curve. After approximately 40 minutes of heating, the specimens were mechanically loaded to failure to investigate the ultimate strength under constant elevated temperature about 1100 ˚C.

For the mechanical loading part, the test specimens were simple supported and vertical loads were applied at two equal distribution points. For a controlled horizontal constraint, each support is attached to a hydraulic actuator, as shown in **Fig. 2**. With this loading system, it was possible to achieve any desired combinations of bending moment and axial force at the segment joint. All the bending moments at the joint sections in this study were the superposition of the moments given by both the vertical loads and the

horizontal forces.

For the present investigation, all tests were conducted under the specified levels of axial compression as an initial condition. This was achieved by applying horizontal loading via the horizontal actuators attached at the end supports to the specified level of compression. At the same time, the vertical load was also applied proportionately so that a desired bending moment level at the joint was established as part of the initial condition. The subsequent mechanical loading test to failure phase was done by increasing the vertical load only, such that the joint was subjected to increasing bending moment under a constant axial force. The general loading condition in a real shield TBM tunnel structure may be characterized by external pressure exerted by the surrounding soil; however, the actual distribution of the pressure load is complicated and could vary from joint to joint. Therefore, in the experiment the external pressure load was simplified into 20, 40 and 60 kN three levels referred to a preliminary hand calculation regarding force equilibrium and pressure stress distribution in ambient temperature. The above considerations formed the primary basis for the experimental setup of the segmental joints and the loading and boundary conditions.

2.3. Main measurements

The structural response of the specimens was measured for the vertical deflections at the mid-span and some selected locations, and the horizontal displacements at the supports. Temperature in the specimens was measured at specific locations by thermal couples, and it was also monitored by a non-contact, high sensitivity infrared radiometer.

As a key response measure, the nominal opening gap and opening angle of the lining

joints in the tests was inferred from a set-up as illustrated in **Fig. 3**. In this set-up a pair of LVDTs was mounted to the measuring arms at two different distances from the segment surface to measure the relative displacements ΔL_1 and ΔL_2. The opening angle and the opening gap may be determined from the relative displacements according to the geometric relationship as:

$$\begin{cases} \theta = 2\arctan\dfrac{\Delta L_1 - \Delta L_2}{2d_1} \\ \Delta_{inside} = (d_2 + H)\times\dfrac{\Delta L_1 - \Delta L_2}{d_1} - \Delta L_2 \\ \Delta_{outside} = d_2 \times\dfrac{\Delta L_1 - \Delta L_2}{d_1} - \Delta L_2 \end{cases} \tag{2}$$

where θ is the opening angle of the lining joints; Δ_{inside} is the opening gap of the lining joints at the heating surface (in mm); $\Delta_{outside}$ is the opening gap (when the value becomes positive) of the lining joints at the unexposed surface; d_1 is the distance between two LVDTs; d_2 is the distance between the second (lower) LVDT and the unexposed surface; ΔL_1 and ΔL_2 are the displacement increments of the first and the second LVDT, respectively; H is the thickness of the tunnel linings.

2.4 Test results

A summary of the maximum load capacities as obtained from the experiment is given is **Table 1**. Comparing specimen RCJ2 under the elevated temperature with the reference specimen RCJ0 under ambient temperature, both with the same axial compression (40 kN), the vertical load resistance capacity reduces to 9.04 kNm in RCJ2 from 11.38 kNm in RCJ0, showing a decrease of about 20%. **Fig. 4** shows the relationships of vertical load vs. vertical displacement and joint bending moment vs. joint opening gap for the two specimens. It can be seen that specimen RCJ2 exhibited generally similar

load-deformation behavior as RCJ0 and the failure mode was also dominated by yielding of the bolts at the joint until the concrete on the compression edge at the joint region crushed. The loading capacity was governed by the maximum bending moment at the joint. The decrease of the bending moment capacity may be explained by the reduction of the yield strength of the bolts under the fire effect.

Comparing the three specimens under the same elevated temperature (RCJ1-3) from **Table 1**, it can be seen that the load resistance capacity tended to increase as the axial compression increased from 20kN, to 40 kN and 60 kN.

3. Thermo-mechanical model for the segmental joint

In this section, a semi-theoretical thermo-mechanical model for simulating the joint behavior in fire is proposed. The model consists of a series of deformation states. Each deformation state corresponds to a load bearing mode of the joint. The contributions of the concrete and bolts in a tunnel fire to the mechanical behavior of the joint are included in the model. The key aspect of the model is in the calculation of the joint rotation stiffness under a given eccentric loading and an elevated temperature effect.

Assuming a general joint model the following standard assumptions are adopted (Ding et al., 2013; Li et al, 2015a, 2015b):

1. The deformation of joint obeys the plain section assumption. In the compressive zone of the joint, the strain along the joint contact surface is assumed to be a plane section.

2. The concrete of joint is considered to be in an elastic state. The rotation angle and deformation of the joint are very small compared with the size of the segment. To

calculate the rotation angle of the joint, the surface of the joint is assumed to be plane before and after bending.

3. The bolt is assumed to bear the tensile stress only, and the concrete is assumed to resist the compressive stress only. In the compressive zone of the joint, the distribution of the strain along the joint contact surface is linear.

The plane joint model without elastic liner is schematically shown in **Fig.6**. The opening angle of the joint can be calculated as:

$$\theta = \frac{\delta_c}{h_c} \tag{3}$$

where δ_c is the deformation in the outer edge of the compressive zone of joint, h_c is the height of the compressive zone.

The bending resistance stiffness of joint (K_θ) can be found by Eq.(4):

$$K_\theta = \frac{M}{\theta} \tag{4}$$

where M is the bending moment of the joint.

For the analysis of the temperature field in fire, concrete is considered as a homogeneous material with the assumption that the presence of the steel bars has little influence on the temperature field of concrete (Lie and Chabot, 1990). For simplification, the thermal parameters of concrete, such as thermal conduction, specific heat, density, thermal diffusivity, and surface heat transfer coefficient, are assumed to be unchanged with temperature. Besides, the thickness of tunnel lining is usually larger than 200 mm, and the thermal conductivity of lining concrete is rather low, hence the influence area of

hot airflow smoke would generally not be beyond the thickness of the tunnel lining. From the perspective of heat transfer, if the thickness of a lining is much greater than the infiltrating depth during the considered time of interest, it could be considered as a semi-infinity medium, and the temperature field can therefore be obtained by the solution of semi-infinity heat conduction theory.

3.1 General temperature boundary condition

The main modes of heat transfer processes include heat conduction, convection, and radiation within or between bodies of matter. Generally, heat conduction and radiation occur in solid matter, and heat convection and radiation occur when solid matter is exposed to fluid flow or other materials. The heat transfer from a heat source to a tunnel lining should ideally include all three major modes of heat transfer, and not be limited to a simple heat conduction analysis (Caner et al., 2005; Pichler et al., 2006).

However, heat transfer by radiation is very difficult to consider, hence a combined heat transfer coefficient is commonly used in the heat transfer analysis of materials in heated air. This is defined as the convective heat transfer coefficient, which takes into account the heat transfer by radiation (Çengel, 2004). The analytic solution for temperature reaction inside the tunnel lining as a semi-infinity medium with the heat convection boundary condition at the lining surface can be expressed as (Holman, 2002):

$$\frac{T(x,t)-T_0}{T_f-T_0}=erfc\left(\frac{x}{2\sqrt{\alpha t}}\right)-[\exp(\frac{hx}{\lambda}+\frac{h^2\alpha t}{\lambda^2})][erfc(\frac{x}{2\sqrt{\alpha t}}+\frac{h\sqrt{\alpha t}}{\lambda})] \quad (5)$$

where $T(x,t)$ is the temperature of the tunnel lining at depth x and time t, $erfc(u)$ is the

Gauss error complementary function, T_0 is the initial temperature of tunnel lining, T_f is the temperature of thermal flue gas flow in fire, h is the surface heat transfer coefficient of the tunnel lining, α is the thermal diffusivity of the lining concrete, and λ is the thermal conductivity of the lining concrete.

In the case of a tunnel fire, the temperature of thermal flue gas flow (T_f) is raised to the highest value regardless of what type of heating curve is used for simulations because quick warming is one of the characteristics of fire disaster occurred in tunnel. On the other hand, owing to the weak thermal conduction of concrete, the thermal flue gas flow can only influence a small part of the thickness inside tunnel lining under warming condition. In order to satisfy boundary condition, T_f is assumed to be the highest value of the heating curve.

3.2 Heat flow invading through the joint

In addition, when the inner side of the joint opens, heat flow spreads in the joint, and this leads to higher temperatures in the concrete in the vicinity of the joint than the concrete in the lining segment. As can be seen in **Fig. 7**, this phenomenon was observed in the test by thermal infrared imager. In order to account for the differences between the temperatures in the concrete at the joint and in the lining segment, a pair of temperature adjustment coefficients, for the concrete at the joint as η and for the joint bolt as ζ, are introduced. When the inner side of the joint remains closed, the gap of the joint is generally insignificant, and so the temperature of the joint can be regarded as equal to the

lining segment, thus η and ζ are both equal to 1.0. When the inner side of the joint opens, η and ζ are greater than 1.0, indicating that the temperature of concrete at the joint is higher than that of concrete of the lining segment.

The above temperature adjustment coefficients for the concrete and the bolt at the joint section can be determined empirically using numerical simulation in conjunction with the data from thermal infrared images captured from physical experiments, as discussed in the following sub-sections.

3.3 Determination of the temperature adjustment coefficient

To assist in the determination of the temperature adjustment coefficient, a numerical model was developed using the finite element method. By employing the sequential coupling method, the standard European HC curve was utilized to simulate the fire performance of segmental joints. The heating curves of concrete and bolts were applied using a predefined heating method. C2D4R elements were used to simulate the concrete. C2D4R was a two-dimensional four-node linear heat conduction unit, which adopts the linear reduction integral of fine mesh division. The degrees of freedom were the temperature at each node in heat conduction simulation analysis. In addition, the degrees of freedom were translational and rotational at each node in stress–displacement simulation analysis of the element. B21 elements were used to simulate the bolts. B21 was a two-node linear beam element that can withstand tensile or compression loads and bending. An ‘embedded’ command was utilized to simulate the interaction between

concrete and the bolt. The embedded element technique is used to specify that an element or group of elements is embedded in "host" elements. If a node of an embedded element lies within a host element, the translational degrees of freedom and radial degree of freedom at the node are eliminated and the node becomes an "embedded node." The translational degrees of freedom and radial degree of freedom of the embedded node are constrained to the interpolated values of the corresponding degrees of freedom of the host element. Embedded elements are allowed to have rotational degrees of freedom, but these rotations are not constrained by the embedding. Multiple embedded element definitions are also allowed. Hence, the embedded element technique can be used to model contact between the bolt and concrete. Moreover, a pinned connection at the end of the segments was used as a boundary condition. The ends of the segments were adiabatic; i.e. they were not heated when the internal temperature varied.

The numerical process is performed in the transient temperature field. The thermal field of the cross-sections is analyzed at each time step and then material properties are adjusted according to the obtained temperatures. Reliable predictions from the FE analysis depend on accurate temperature-dependent material properties. The detailed time-dependent specific heat and thermal conductivity values were calculated with the experimental relationships proposed in Eurocode 2 (CEN, 2004; 2005). Referring to test results, the geometry parameters were determined by the experimental investigation from Yan et al. (2016).

The input parameters of concrete are listed in **Table 2**. In the FE model, the

boundary conditions were applied according to those of segmental joints in tunnel fire. Generally, a tunnel segmental joint is assumed to be heated only from the bottom, while the joint side is also heated under the heating flow invasion. A two-dimensional model was created and meshed using continuum two-dimensional heat-transfer elements in FEM software using the implicit solver. During this process, the joint is divided into a number of elements along its thickness and length. The density and shape of mesh division were required by the finite element calculation. A relatively convergent solution can be obtained by trial calculation of different meshing densities to reach reasonable accuracy results. To determine a suitable mesh size, a mesh-sensitive study was conducted. Temperature results did not change when the mesh size decreased from 0.01 to 0.005 m. Based on the influence of different cell types and mesh density of concrete temperature field, structural grid generation technology was adopted, and the grid size was 0.01m. At this point, nodal solution of adjacent elements of nodes derived from stress and strain and the element solution by the strain and stress matrix of each element were used. In this way, the element solution and nodal solution at the corresponding position in the whole loading process were consistent (Wu et al., 2015, 2020). A typical FE model of a one-side heated joint is shown in **Fig. 8**.

The comparison of the segment temperature time histories between numerical and test results are shown in **Fig.9**. The main difference is due to a temperature plateau, during which the temperature tended to hold, and this appears in the time-temperature curves when the temperature in the concrete at the measured locations reached around 100 ˚C (or

slightly higher). This phenomenon may be attributed to the effect of evaporation of free water and chemically bonded water of the calcium silicate hydrate (C-S-H) of the lining concrete. The concrete temperature then continued to increase until the endothermic evaporation terminated. The temperature distribution of the half joint after one hour's heating with or without heating flow invasion are shown in **Fig.10**. Compared with the thermal infrared image shown in **Fig.7**, the numerical simulation well reproduces the phenomena of the heat flow invading. Other than the layered temperature distribution in segment, the heating flux invasion changes the layered temperature distribution and notably expands the elevated temperature region and jeopardizes the bolt and surrounding concrete.

The time histories of average temperature of joint section concrete with or without heating flow invasion are shown in **Fig.11**. The average temperature only reaches approximately 150 ℃ in two hours. Compared with the heating flow invasion case, heating flow to the joint significantly raises the temperature and the temperatures reach 500 ℃ and 700 ℃, in one hour and two hours respectively. The time histories of the average temperature of joint bolts with or without heating flow invasion are shown in **Fig.12**. Based on the numerical results, the heating flow invasion obviously influences the elevated temperature level of the bolt. The average temperature of the joint bolt with heating flux invasion is 200 ^{0}C higher than that without heating flux invasion. According to the temperature variation results, the temperature adjustment coefficients of the joint concrete η and the joint bolt ζ are obtained and these are presented in **Fig.13** and **Fig.14**.

Both adjustment coefficients in different times are referred to in the calculation of the rotational stiffness of the segmental joint in fire in Section 4.

4 Rotational stiffness of the segmental joint in fire

4.1 Calculation of rotational stiffness of the segmental joint in fire

The key point of the model is about the calculation of the joint rotation stiffness. As shown earlier in **Fig.6**, the joint rotation is determined by the deformation in the outer edge of the compressive zone of the joint and the height of the compressive zone. The latter two factors are the deformation response under a given eccentric loading and an elevated temperature effect. The calculation model consists of a series of deformation states. Each deformation state corresponds to a load bearing mode of the joint. The contributions of the concrete and bolts in a tunnel fire to the mechanical behaviour of the joint are included in the model. The stress distribution of the concrete compressive zone can be obtained by the force equilibrium and geometric compatibility under the assumption of a rectangular or a parabolic distribution of the stress. A schematic of the general force diagram is shown in **Fig.15**. The force equilibrium equation is expressed as Eq. (6):

$$\begin{cases} N + nF_b - C_1 = 0 \\ M + nF_b h_b + N\dfrac{H}{2} + M_{C1} = 0 \end{cases} \tag{6}$$

where N is the axial force; M is the bending moment; n is the number of bolts (generally two); Point ***O*** and Point ***A*** are respectively the inner and outer edge points; h_b is the height

from bolt to Point ***O***; H is the thickness of lining; F_b is the tension force supported by one bolt (ignoring the pre-tightening force); C_1 is resultant force of joint-concrete compressive zone; M_{C1} is the bending moment of C_1 to Point ***O***. The position of opening angle produced by joint section is influenced by different directions of the bending moment supported by the joint. C_1 and M_{C1} also depend on the direction of the bending moment.

The determination of C_1 and M_{C1} are very important for solving the opening angle and the flexural stiffness. For the joint section under full pressure (which mean the entire section is in compression) and hogging moment, the heating flow invasion will not occur. The strain distributions of the joint section under full pressure and hogging moment are shown in **Fig.16 and Fig.17(a)**, respectively. The determination of C_1 and M_{C1} are given by Eq. (7) and Eq. (8), respectively. It should be noted that the joint rotation does not occur under full pressure.

$$\begin{cases} C_1 = b\int_0^H \left[E_c\left(x,T\right)\cdot\left(\dfrac{\varepsilon_t-\varepsilon_a}{H}x+\varepsilon_t\right)\right]dx \\ M_{C1} = b\int_0^H \left[E_c\left(x,T\right)\cdot\left(\dfrac{\varepsilon_t-\varepsilon_a}{H}x+\varepsilon_t\right)x\right]dx \end{cases} \quad \text{(under full pressure)} \tag{7}$$

$$\begin{cases} C_1 = b\int_0^{h_c} \left[E_c\left(x,T\right)\cdot\dfrac{\varepsilon_c}{h_c}\left(h_c-x\right)\right]dx \\ M_{C1} = b\int_0^{h_c} \left[E_c\left(x,T\right)\cdot\dfrac{\varepsilon_c}{h_c}\left(h_c-x\right)x\right]dx \end{cases} \quad \text{(under hogging moment)} \tag{8}$$

where b is the width of the segmental joint, ε_a is the maximum strain of the compression zone under full pressure; ε_t is the minimum strain of the compression zone under full pressure; ε_c is the strain of edge point of compression zone; h_c is the height of compression zone. $E_c(x,T)$ is the elastic modulus of the concrete at the height x under temperature T,

which is determined by Eq. (5).

The strain distributions of the joint section under a sagging moment are shown in **Fig.17(b)**. For the joint under a sagging bending moment, with heating flow invasion effect, C_1 and M_{C1} are shown as Eq. (9):

$$\begin{cases} C_1 = b\int_{H-h_c}^{H}\left[E_c\left(x,\eta T\right)\cdot\dfrac{\varepsilon_c}{h_c}\left(x-\left(H-h_c\right)\right)\right]dx \\ M_{C1} = b\int_{H-h_c}^{H}\left[E_c\left(x,\eta T\right)\cdot\dfrac{\varepsilon_c}{h_c}\left(x-\left(H-h_c\right)\right)x\right]dx \end{cases} \quad \text{(under sagging moment)} \qquad (9)$$

The relationship of tensile force and the deformation of the bolt is given in Eq (10), and the relationship of the deformation in the outer edge of the compressive zone of joint and the bolt is given in Eq. (11) based on the plane cross-section assumption. When the joint is under full pressure, i.e. the joint maximum joint opening width is zero, F_b=0.

$$F_b = A_b E_b\left[\xi T\left(h_b,t\right)\right]\varepsilon_b \qquad (10)$$

$$\delta_c = \frac{h_c}{h_b-h_c}\delta_b = \frac{h_c}{h_b-h_c}\varepsilon_b l_b \qquad (11)$$

where ε_b and l_b is the tensile strain and the length of the bolt, respectively; $E_b(x,T)$ is the elastic module of the bolt under temperature T.

δ_c and h_c can be obtained from Eq. (6) (10) (11) in conjunction with the corresponding distribution of the temperature adjustment coefficient. Afterwards, according to Eq. (3) and Eq. (4), the opening angle θ and the flexural stiffness K_θ can be worked out.

4.2 Comparison between predictions and test results

The analysis procedure in Section 4 is verified with the experimental results. The input parameters of the specimens are as described in Section 2.1. The calculated bending moment vs opening angle of the segmental joint in different axial level cases, i.e., the

comparison between M-θ curves of experimental and analytical models RCJ1, RCJ2 and RCJ3 under fire are shown in **Fig.18**. It can be seen that the analysis gives good prediction of the experimental observation. The M-θ curves of the joints under fire still follow generally an approximate bi-linear form, and the patterns of the experimental results are reasonably reproduced using this model. The bending moment at the intersection point of the M-θ curves increases with the increase of the axial force level.

As can be seen in **Fig.18**, the calculated bending moment at each joint angle tends to be smaller than the corresponding test value, especially for RCJ3, and this difference becomes larger with the increase of the joint angle. For the specimens tested to failure under elevated temperatures, failure occurred in a tensile bending mode with extensive yielding and joint gap openings before final crushing of concrete at the top side, except for RCJ3 where compressive bending failure occurred due to a higher axial load. The 10% deviation may be attributed to simplifications in the numerical modeling and some complexities in the actual test specimens such as the nonlinear behaviour of materials and contact surface interactions, especially during heating at elevated temperatures. Nevertheless, the analytical model is capable of imposing the mechanical and thermo boundary conditions to predict the overall performance of the tunnel segmental joint in fire, and because of its simple procedure this method can be applied conveniently in the fire resistance design of the segment joints in the shield tunnel lining.

5 Parametric study

As the presented model in previous session has been proved to be accurate and reliable in analyzing the behavior of a segmental joint at elevated temperature, this model is used to carry out a parametric study to investigate the effect of some key parameters. In the parametric study, the model is heated in the standard European HC curve heating process. The general tunnel lining structure of Metro Lines in Shanghai is taken. The parameters for the calculation are listed as follows:

(1) heating condition: in one hour's heating phase of the standard European HC curve (except for the cases under the different heating curve)

(2) concrete: Type C55, f_c = 25.3 MPa;

(3) segment joint: the thickness of the segment H=350mm, b=1200mm., the distance from the bolt to the external edge of the segment h_b is 230mm, i.e. the bolt location is measured by the distance from its axis to the internal edge of the segment is 120mm (except for the cases with different bolt locations).

(4) bolt: The bolt grade is 5.8, which means its elastic module E_b is 210 GPa and its yield strength f_y is 400 MPa. The length of the bolt l_b is 472 mm. The full cross-sectional area of the bolts A_b is 1418 mm^2 (2 bolts).

(5) load: We gradually increase the bending moment level and remain the axial load. The initial axial load is 1000kN (except for the cases with different the initial axial loads).

5.1 Influence of the heating curve

Commonly prescribed structural design fires used are generally defined by time–temperature curves. In the fire safe design of structures, the design fires represent the range of credible scenarios necessary to evaluate the performance of the structure, whilst attempting to adequately account for the possible maximum influence of the of typical tunnel fires (Beard and Carvel, 2005; Maluk et al., 2019). To evaluate the rotation stiffness of segmental joint in fire for one hour's heating, the standard European HC curve was employed to simulate the heating phase according to Eq (1). As a contrast, we also employed the RABT curve (SFPE, 2004) in heating phase as shown in Eq. (12):

$$T(t)=\begin{cases}20+236t & 0\le t\le 5\\ 1200 & 5\le t\le 60\end{cases} \tag{12}$$

The relationships of joint rotation angle versus sagging moment and hogging moment with different heating curves are shown in **Fig. 19**. The fire exposure leads to reduction of load-carrying capacity and stiffness, but as for thermo plastic strain expands, an increase of the displacement corresponding to peak load (Liu et al., 2021). Along with the bolt tension and yielding, the M-θ curves in ambient temperature depict that the rotation stiffness of the joint varies with the increasing load under both sagging and hogging moments. Combining with the analysis in the experimental study shown in **Fig. 18**, the mechanical behavior of the segmental joint can be divided into three stages: (i) In the first stage, entire the concrete contact surface of the joint is still closed, no obvious joint opening is observed. (ii) In the second stage, the concrete contact surface of the joint is gradually opened from internal or external side, and an obvious joint opening is observed, and the heat flow invasion gradually develops. A growing tensile force in the bolt magnifies the thermo-mechanical degrading. (iii) Finally, the bolt strain exceeds its

yield strain, and the joint completely damages when the concrete in this area suddenly crushes. Moreover, the heating damage and heat flow invasion shorten the second stage and induce the M-θ curves turn to approximate bi-linear shapes. The safety capacity for the stiffness is weaken compared with the ambient case. As for more adverse heating condition of the RABT curve, the joint suffered more reduction of the capacity and stuffiness than that under the standard European HC curve. In contrast, the influence of two heating curve is more obvious under sagging moments than hogging moments. That can be attributed to the heat flow invasion to the opening joint is a key factor affecting the mechanical properties. The heat flow invasion intensifies the thermo damage to the bolts with opening width under sagging moments. In contrast, the mechanical behavior of joints under hogging moments are mainly influenced by the degrading of concrete exposing to fire.

5.2 Influence of the bolt location

The influence of the bolt location on the behavior of the joint is also investigated due to the bolt is the only structural component that bears the tensile force and is more vulnerable in fire. The relationships of joint rotation angle versus sagging moment and hogging moment with different bolt locations of 90, 120 and 150 mm are shown in **Fig. 20**. The bolt location also has a significant influence on the joint mechanical behavior in fire. For the sagging moment case, the closer the bolt is located to the internal edge, the smaller the joint opening angle is. As for hogging moment case, the closer the bolt is located to the internal edge, the larger the joint opening angle is. Based on the effective section height,

we can find when the bolt is located closer to the internal edge, the bearing capacity is increased for the joint subjected to a sagging moment and decreased for the joint subjected to a hogging moment. The closer the bolt is located to the internal edge, the larger the bending moment are in the ultimate limit state for the sagging moment case, and the smaller the bending moment are in the ultimate limit state for the hogging moment case. When the distance of the bolt to the internal edge decreases from 90 to 150 mm, the ultimate limit bending moment decreases by 5% for the sagging moment case and increases by 15.8% for the hogging moment case. Furthermore, the heat flow invasion effect gradually weakens with the bolt location move away from the heating side in sagging moment case. And the compressive zone of concrete degrading in fire induces more reduction of the capacity and the rotation stiffness for the case with lower effective section height under hogging moments.

5.3 Influence of the axial load

With regard to the structure in fire, the effect of the boundary conditions is quite important, with a stronger increase for more restraint boundary conditions (Mohammadbagheri and Shekastehband, 2020). To illustrate the effect of the boundary conditions, the influence of the axial load on the mechanical behavior of the joint is investigated. The relationships of joint rotation angle versus sagging moment and hogging moment with different axial loads of 500, 1000 and 1500 kN are shown in **Fig. 21**. The axial load has a significant influence on the bearing capacity of the joint for both cases. The larger the axial load is, the smaller the joint opening angle is for both the sagging

moment case and hogging moment case. The bending moment in the ultimate limit state increases by 12~23.7% for the sagging moment case and increases by 26~35% for the hogging moment case with the increasing of the axial load by 500 kN. The case with 1500kN axial load under sagging moments demonstrates more robustness with bending moment increasing, while the cases with 500kN and 1000kN axial loads collapse when the bolts enter the yielding stage.

5.4 Discussion

The previous analyses unequivocally show that the different heating curves, the bolt locations and the initial axial loads, all have a significant influence on the bending stiffness of the segmental joint. More specifically, the results obtained from the parametric study indicate that the bending stiffness of the segmental joint increases with the relative bolt locations and the initial axial loads, and decreases with the heating temperatures. Comparatively, the bending stiffness of the joint in sagging moments is more influential than that in hogging moments because of the heating flux invasion as illustrated in **Figs. 11 and 12**.

All the parametric analyses performed show that the bending stiffness of the segmental joints in fire is significantly smaller than that in ambient temperature, especially in the case of the heating flux invasion. This is an important finding because the bending stiffness of the segmental joints has a significant influence on the parameter determination and structural design of the tunnel for fire loadings. A lower stiffness may result in larger deformations, and thus service performance of the shield tunnel in fire, e.g. the joints

water proofing may be compromised, and water gushing occurs. On the other hand, a higher stiffness would lead to larger stresses to the tunnel structure; therefore neglecting the joints may lead to a conservative design of the tunnel structure in fire.

6 Conclusions

The resistance and deformation behaviour of shield TBM tunnel lining under elevated temperature are complicated, and there has been a lack of effective method to quantify the behavior of the segmental joints, which plays a key role in influencing the overall behaviour of the TBM tunnel lining. This paper presents a Semi-analytical thermo-mechanical model for segmental joints exposed to elevated temperatures due to fire. Based the testing and calculated results, the following conclusions can be drawn:

(1) The calculation model has been verified against experimental data from testing of segmental joints under elevated temperature, showing a satisfactory agreement. Both experimental observations and the analytical prediction using the proposed model show that the M-θ curves of the joints under fire follow generally an approximate bi-linear relationship, and the bending moment at the intersection point of the M-θ curves increases with the increase of the axial force level.

(2) According to experimental observation and the analysis in the parametric study, the mechanical behavior of the segmental joint can be divided into three stages: (i) In the first stage, entire the concrete contact surface of the joint is still closed, no obvious joint opening is observed. (ii) In the second stage, the concrete contact surface of the joint is gradually opened from internal or external side, and an obvious joint opening is observed,

and the heat flow invasion gradually develops. A growing tensile force in the bolt magnifies the thermo-mechanical degrading. (iii) Finally, the bolt strain exceeds its yield strain, and the joint completely damages when the concrete in this area suddenly crushes. Moreover, the heating damage and heat flow invasion shorten the second stage and induce the M-θ curves turn to approximate bi-linear shapes.

(3) The proposed analytical model is suitable and convenient for the analysis of shield tunnel lining segmental joints in fire conditions in design applications. The bolt location has a significant influence on the joint mechanical behavior. When the bolt is located closer to the internal edge, the bearing capacity is increased for the joint subjected to a sagging moment and decreased for the joint subjected to a hogging moment. The increase of axial load also has a positive influence on the rotation stiffness and bearing capacity of the joint for both the sagging and hogging moment cases.

To include 3D numerical studies that can be of added value it would require comprehensive model development, validation and parametric calculations, and will therefore extend beyond the current scope of the paper. Hence it would be appropriate to present 3D numerical simulation in a follow-up study,

Acknowledgements

The authors wish to acknowledge the sponsorship from National Key R&D Program of China（2018YFB2101000）, Shanghai Sailing Program (20YF1451400), and the Research Fund of State Key Laboratory for Disaster Reduction in Civil Engineering (SLDRCE19-A-14).

References

Arnau O. and Molins C. Experimental and analytical study of the structural response of segmental tunnel linings based on an in situ loading test. part 2: numerical simulation, 2011, 26(6), 778.

Beard A. and Carvel R. The handbook of tunnel fire safety. Thomas Telford, 2005.

Blom C. B. M. Design philosophy of concrete linings for tunnels in soft soils. TU Delft, Delft University of Technology, 2002.

Cafaro E. and Bertola V. Fires in tunnels: experiments and modelling. Open Thermodynamics Journal, 2010, 4(1).

Caner A., Böncü A. Structural fire safety of circular concrete railroad tunnel linings. Journal of structural engineering, 2009, 135(9): 1081-1092..

Ding W. Q., Peng Y. C., Shen B. W., Yan Z.G., Zhu H. H., Wei, X. X. Full-Scale Test and Modeling on Bending Stiffness of Segment Joint of Shield Tunnel Lining. Journal of Structural Engineering and Mechanics, 2013, 45(3): 333-350

Ding W. Q., Yue Z. Q., Tham L. G., Zhu H. H.; Lee C. F. Analysis of shield tunnel. International journal for numerical and analytical methods in geomechanics, 2004, 28(1), 57-91.

Do N. A., Dias D., Oreste P., Djeran-Maigre I. 2D numerical investigation of segmental tunnel lining behavior. Tunnelling and Underground Space Technology, 2013, 37, 115-127.

El Naggar H. and Hinchberger S. D. An analytical solution for jointed tunnel linings in elastic soil or rock. Canadian Geotechnical Journal, 2008, 45(11), 1572-1593.

CEN, Eurocode 2. Design of concrete structures. Part 1-2: General rules-structural fire design (BSEN1992-1-2, pp. 23–28). London: British Standards Institution, 2005.

Holoman J. P.. Heat Transfer. McGraw-Hill Education, New York, 2002,139-141.

Hao J., Yu K., Gong Q., Zhou S. Load-carrying capability of shield tunnel damaged by shield shell squeezing action during construction. Thin-Walled Structures, 2018, 132, 69-78.

Huang H., Shao H., Zhang D., and Wang F. (2016). Deformational responses of operated shield tunnel to extreme surcharge: a case study. Structure and Infrastructure Engineering 13, 345-360.

Kim J. H. J., Lim Y. M., Won J. P., Park H. G. Fire resistant behavior of newly developed bottom-ash-based cementitious coating applied concrete tunnel lining under RABT fire loading. Construction and Building Materials, 2010, 24(10), 1984-1994.

Koyama Y. Present status and technology of shield tunneling method in Japan. Tunnelling and Underground Space Technology, 2003, 18(2), 145-159.

Lee K. M., Ge X. W. The equivalence of a jointed shield-driven tunnel lining to a continuous ring structure. Canadian Geotechnical Journal, 2001, 38(3), 461-483.

Li X. J., Yan Z. G., Wang Z., Zhu H. H. Experimental and analytical study on longitudinal

joint opening of concrete segmental lining. Tunnelling and Underground Space Technology, 2015a, 46, 52-63.
Li X. J., Yan Z. G., Wang Z., Zhu H. H. A progressive model to simulate the full mechanical behavior of concrete segmental lining longitudinal joints. Engineering Structures, 2015b, 93, 97-113.
Lie T. T., Chabot M. A method to predict the fire resistance of circular concrete filled hollow steel columns. Journal of fire protection Engineering, 1990, 2(4), 111-124.
Liu F, Yang H, Wang W. Behaviours of concentrically and eccentrically loaded square steel tube confined reinforced concrete slender columns after fire exposure[J]. Thin-Walled Structures, 2021, 158: 107155.
Maluk C., Bisby L., Krajcovic M., Torero J. L. A Heat-Transfer Rate Inducing System (H-TRIS) Test Method. Fire Safety Journal. 2019, 105: 307-319.
Mohammadbagheri S, Shekastehband B. Fire resistance of stiffened CFDST columns after earthquake-induced damages. Thin-Walled Structures, 2020, 154: 106865.
SFPE, SFPE Engineering Guide to Fire Exposure of Structural Elements, Society of Fire Protection Engineers, USA, 2004.
Teachavorasinskun S., Chubuppakarn T. Influence of segmental joints on tunnel lining. Tunnelling and Underground Space Technology, 2010, 25(4), 490-494.
Vianello C., Fabiano B., Palazzi E., Maschio G. Experimental study on thermal and toxic hazards connected to fire scenarios in road tunnels. Journal of Loss Prevention in the Process Industries, 2012, 25(4),718–29.
Wen B., Wu B., Niu D. Post-earthquake fire performance of reinforced concrete columns. Structure and Infrastructure Engineering, 2015, 12, 1106-1126.
Wen B., Zhang L., Wu B., Niu D. High-temperature performance of damaged reinforced concrete columns under post-earthquake fires. Structure and Infrastructure Engineering, 2020, (3), 1-15.
Yan Z., Zhu H., Ju J. W., Ding W. Full-scale fire tests of RC metro shield TBM tunnel linings. Construction and Building Materials, 2012, 36, 484-494.
Yan Z, Zhu H, Ju J W. Behavior of reinforced concrete and steel fiber reinforced concrete shield TBM tunnel linings exposed to high temperatures. Construction and Building Materials, 2013, 38, 610-618.
Yan Z., Shen Y., Zhu H., Li X., Lu Y. Experimental investigation of reinforced concrete and hybrid fibre reinforced concrete shield tunnel segments subjected to elevated temperature. Fire Safety Journal, 2015,71, 86-99.
Yan Z., Shen Y., Zhu H., Lu Y. Experimental study of tunnel segmental joints subjected to elevated temperature. Tunnelling and underground space technology, 2016, 53, 46-60.
Yan Z., Zhang Y., Shen Y., Zhu H., Lu Y. A multilayer thermo-elastic damage model for the bending deflection of the tunnel lining segment exposed to high temperatures. Tunneling and Underground Space Technology, 2020, 95, 103142.
Yasuda F., Ono K., Otsuka T. Fire protection for TBM shield tunnel lining. Tunneling and Underground Space Technology. 2004, 19: 4-5.

Zhang W., Koizumi A. A study of the localized bearing capacity of reinforced concrete K-segment. Tunneling and Underground Space Technology, 2007, 22(4): 467-473.

Zhao J., Zheng J. J., Peng G. F., Breugel K. Numerical analysis of heating rate effect on spalling of high-performance concrete under high temperature conditions. Construction and Building Materials, 2017, 152, 456-466.

Zhong X, Zhu W, Huang Z, Han Y. Effect of joint structure on joint stiffness for shield tunnel lining. Tunneling and Underground Space Technology, 2006, 21(3), 406-407.

Zhu, H. H. Designs and analysis on underground structures. Geo-research Institute Report, Osaka, Japan, 1995.

Table 1

Details of the test arrangement and test results

No.	Initial boundary conditions	Designed loading case	Fire load	M_{max}(kN.m)
RCJ0	M_c =0, p_H=40 kN	LC	HC	M_c=11.38
RCJ1	M_c =0, p_H=20 kN	LC	HC	M_c=6.14
RCJ2	M_c =0, p_H=40 kN	LC	HC	M_c=9.04
RCJ3	M_c =0, p_H=60 kN	LC	HC	M_c=15.26

Note: M_c = bending moment at joint (centre of specimen)

Table 2

Input parameters for thermal analysis (Eurocode 2, 2005)

Input parameters (concrete properties)	Unit	Input values
Heat capacity, c_c	J/kg·K	$c_c = \begin{cases} 900+80\left(\frac{T}{120}\right)-4\left(\frac{T}{120}\right)^2 & 20^\circ\text{C} \le T \le 100^\circ\text{C} \\ 900+(T-100) & 100^\circ\text{C} \le T \le 200^\circ\text{C} \\ 1000+(T-200)/2 & 200^\circ\text{C} \le T \le 400^\circ\text{C} \\ 1100 & 400^\circ\text{C} \le T \le 1200^\circ\text{C} \end{cases}$
Thermal conductivity, λ_c	W/m·K	$\lambda_c = 2-0.2451\frac{T}{100}+0.0107\left(\frac{T}{120}\right)^2 \quad 20^\circ\text{C} \le T \le 1200^\circ\text{C}$
Unit weight, ρ_c	kg/m^3	2300

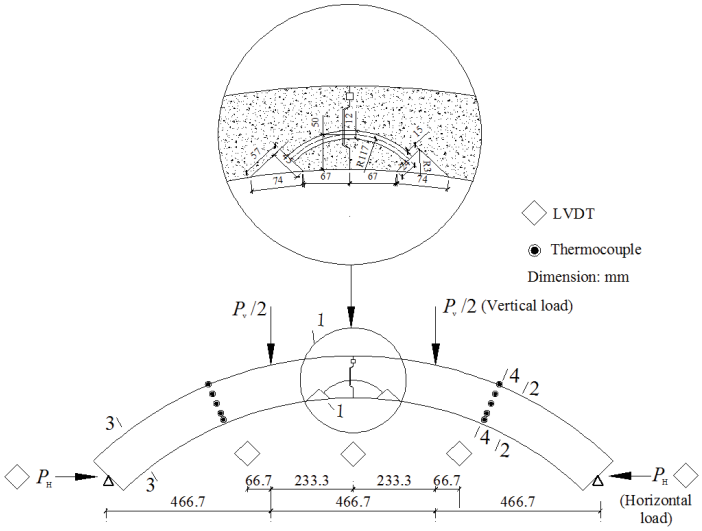

(a)

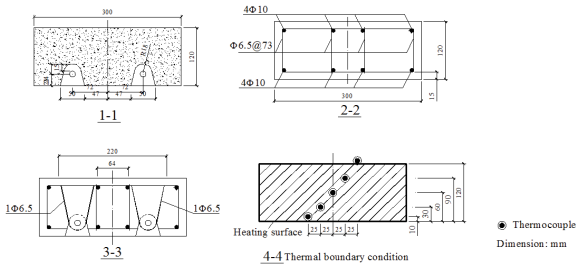

(b)

Fig.1. Configuration of joint assembly, reinforcement arrangement for the RC lining segmental joints, and instrumentation:(a) joint layout; (b) profiles

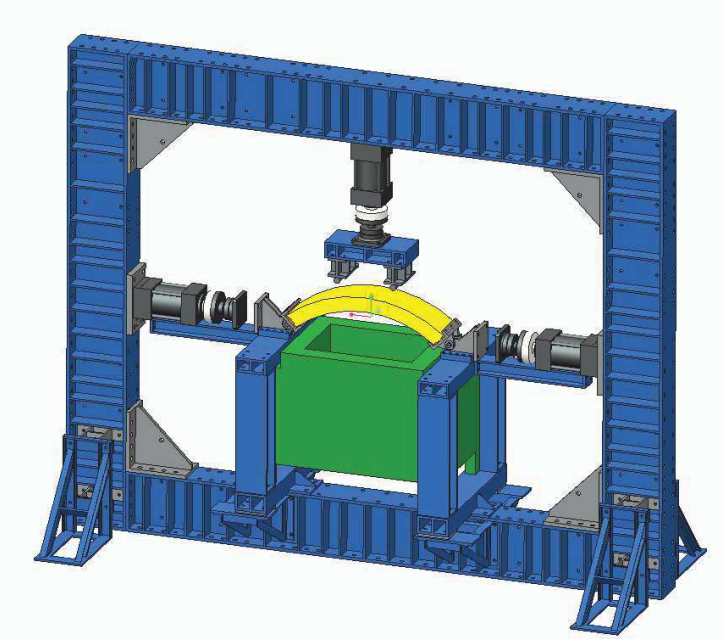

Fig.2. Test setup for combined mechanical and thermal loadings of shield TBM tunnel segments and joints

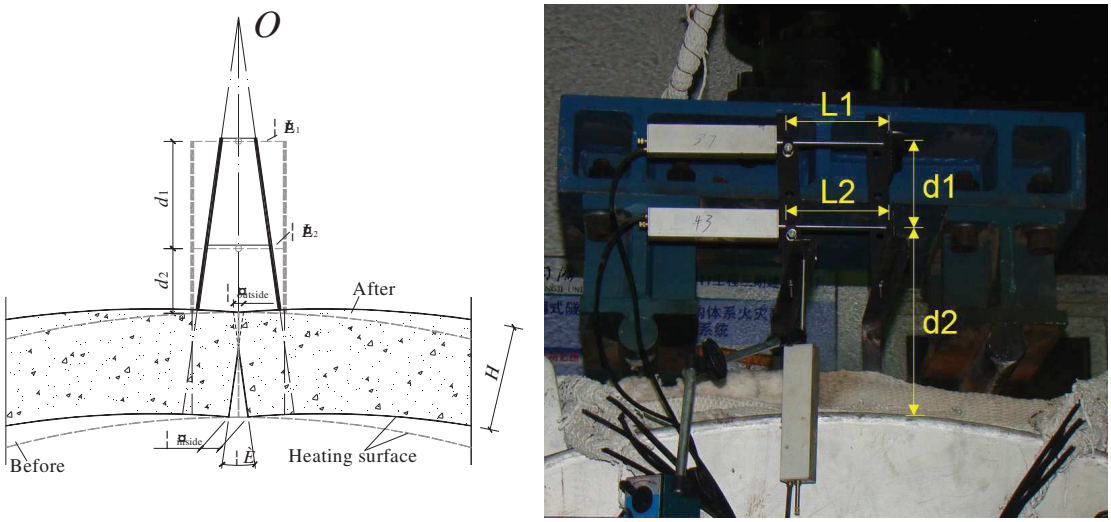

(a) (b)

Fig.3. Measurement of opening angle of the lining joints

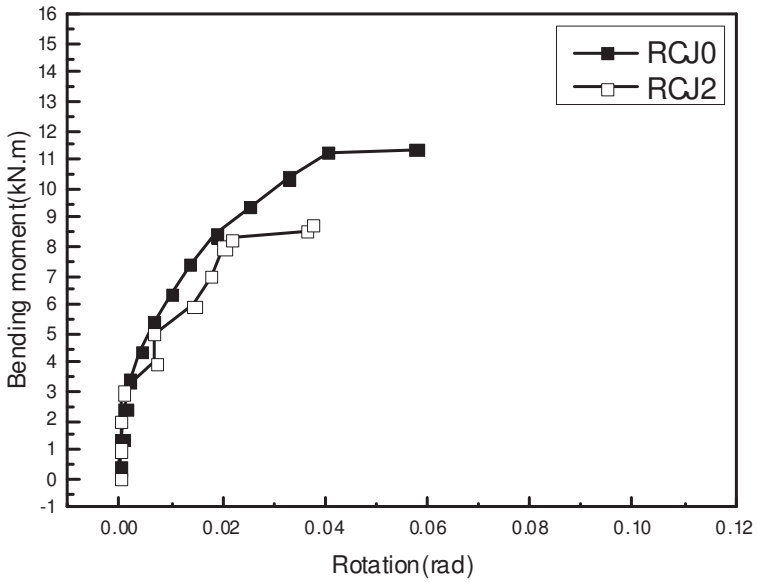

Fig.4. Joint bending moment vs. rotation for RCJ0 & RCJ2 (PH=40 kN)

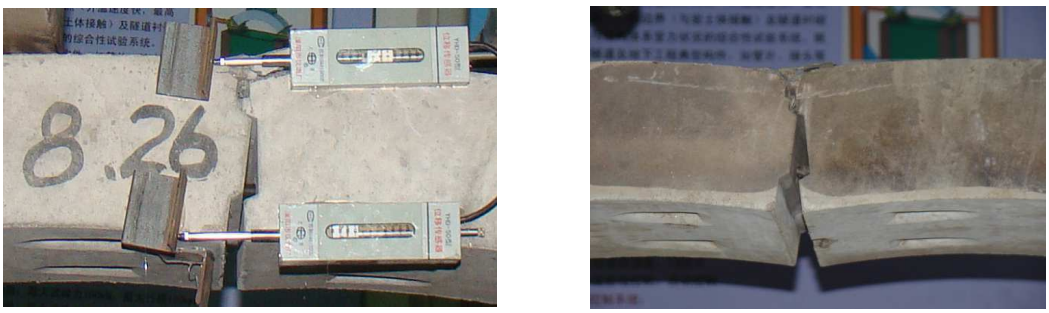

(a) RCJ0 (b) RCJ2

Fig.5. Failure modes of specimens tested at ambient temperature and under fire (for RCJ0 & RCJ2)

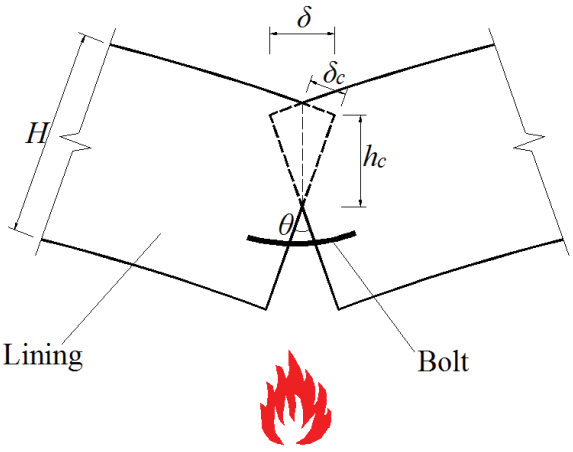

Fig.6. Schematic of the model in sagging moment condition

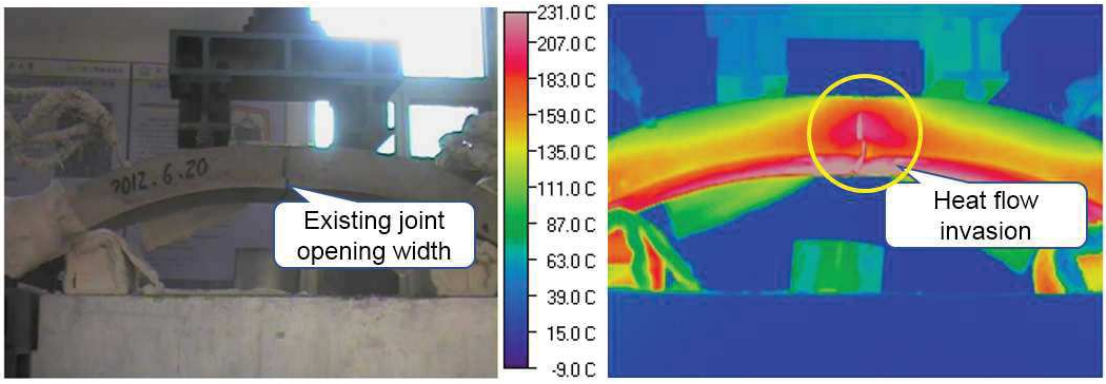

Fig.7. Heat flow invasion phenomenon: evidence from the thermal infrared image

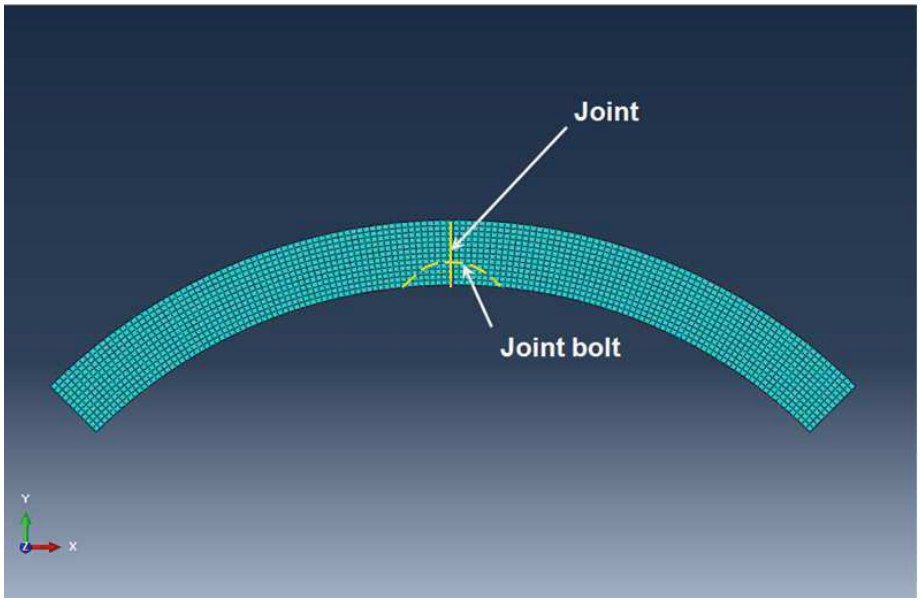

Fig.8. The geometry of numerical model of the segmental joint

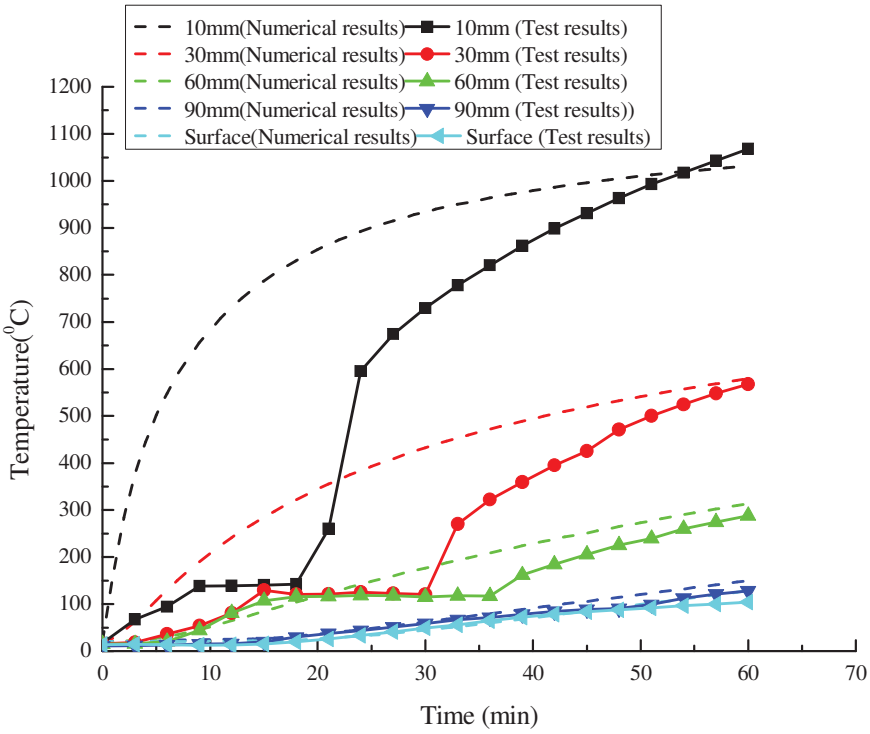

Fig.9. Comparison of the segment temperature time histories between numerical and test results

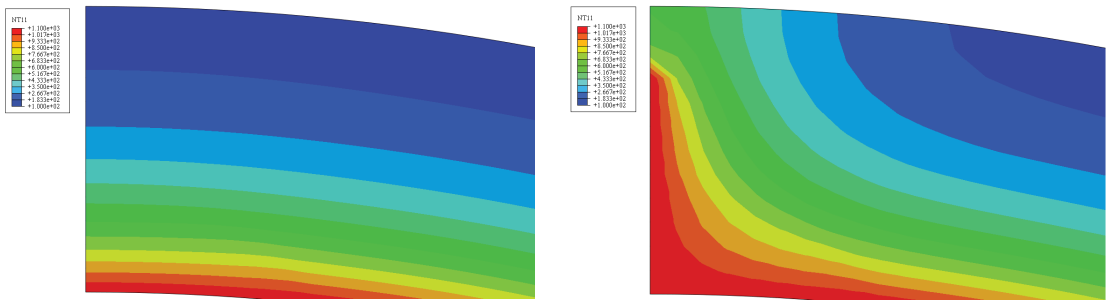

(a) (b)

Fig.10. Cross-section temperature distributions after one hour's heating: (a) without heating flux invasion; (b) with heating flux invasion

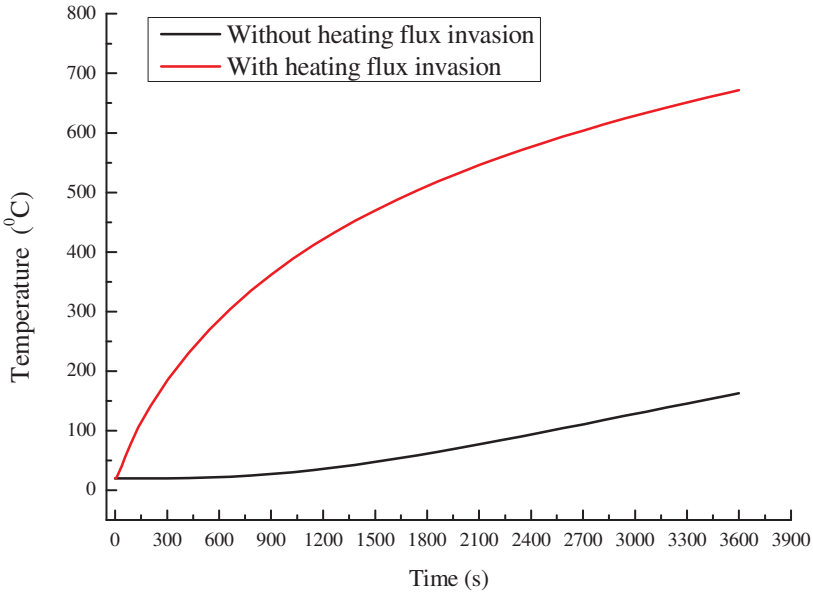

Fig.11. Time histories of average temperature of joint section concrete with or without heating flux invasion

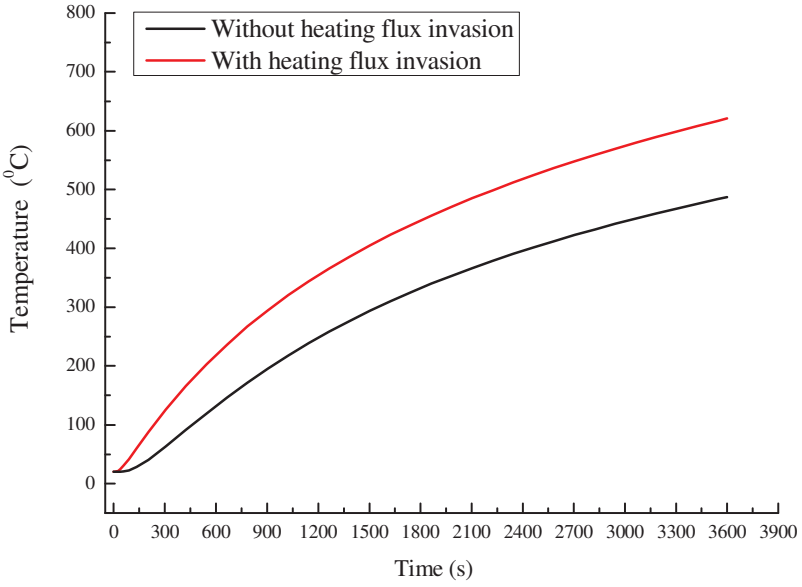

Fig.12. Time histories of the average temperature of joint bolts with or without heating flux invasion

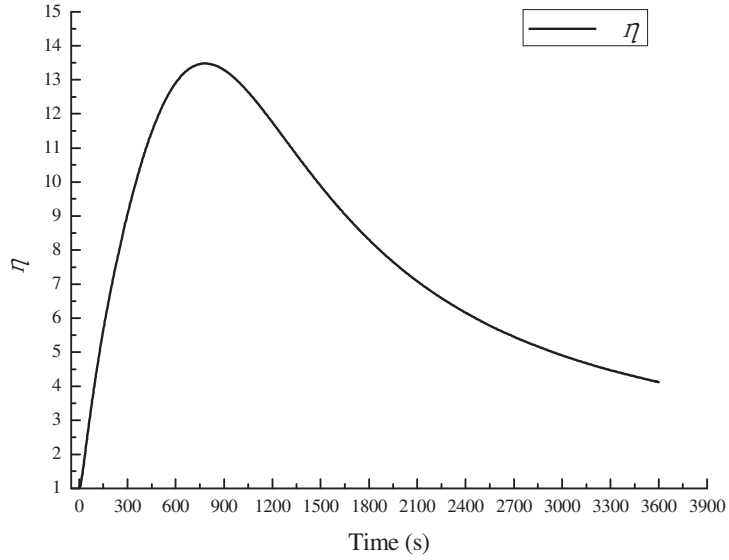

Fig.13. Temperature adjustment factor for the concrete section of the joint

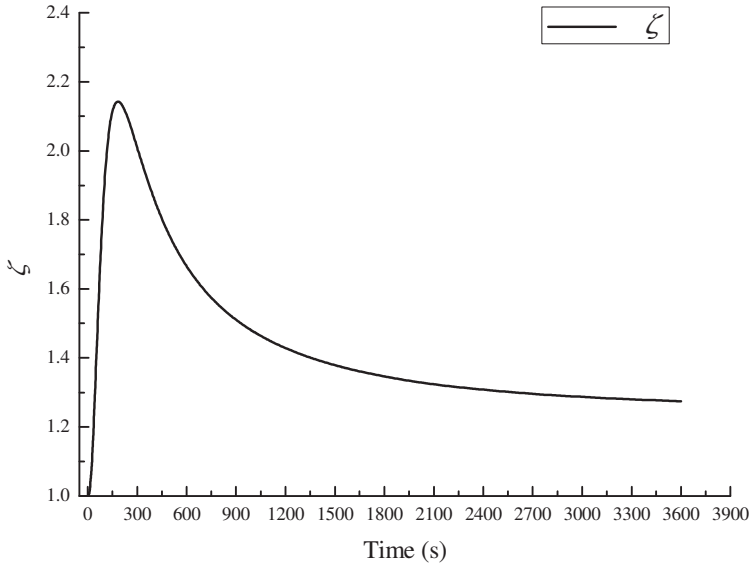

Fig.14. Temperature adjustment factor for the joint bolt

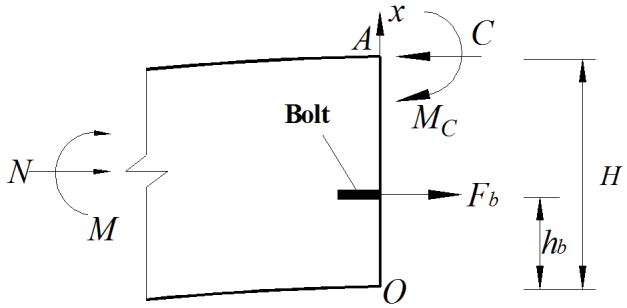

Fig.15. Force schematic diagram

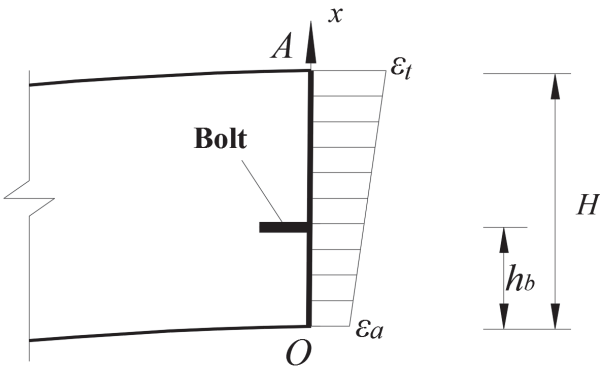

Fig.16. Strain distribution of joint section under full pressure

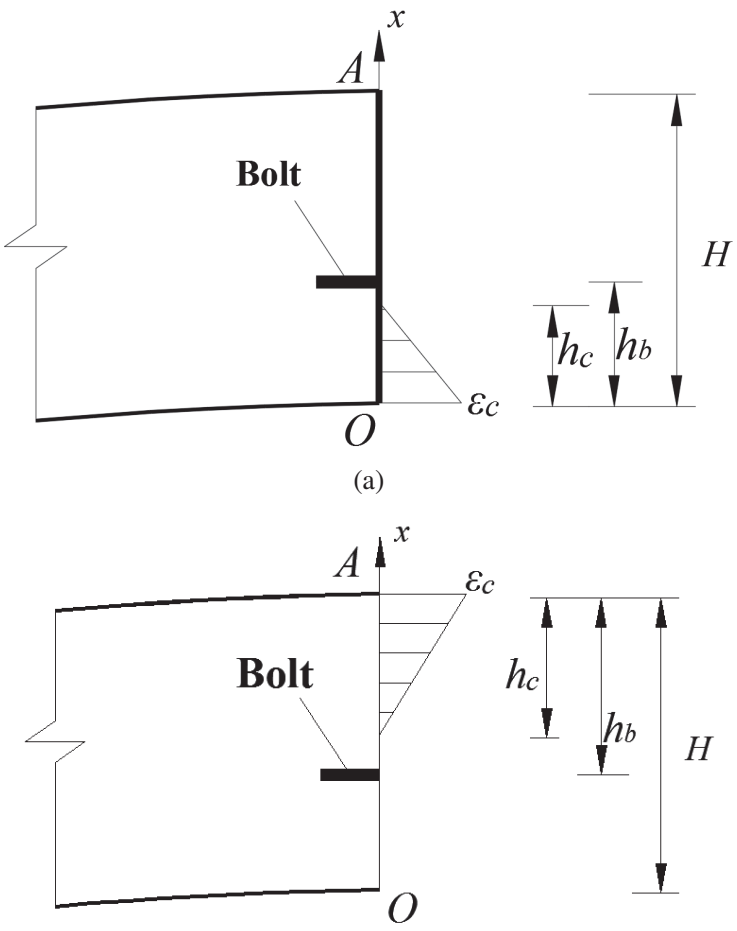

Fig.17. Strain distribution of joint section (a) under hogging bending moment; (b) under sagging bending moment

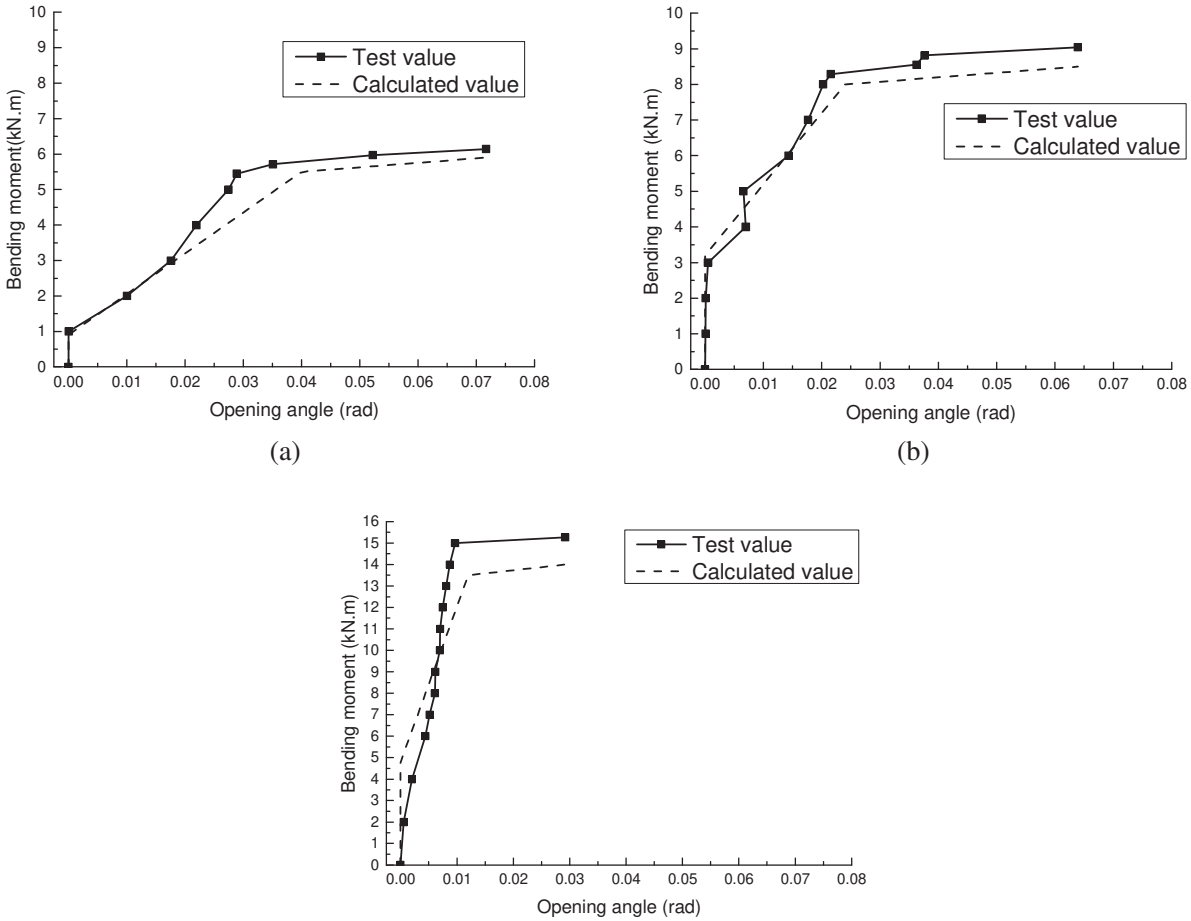

Fig.18. Comparison between *M*-θ curves of experimental and analytical models: (a) RCJ1; (b) RCJ2; (c) RCJ3

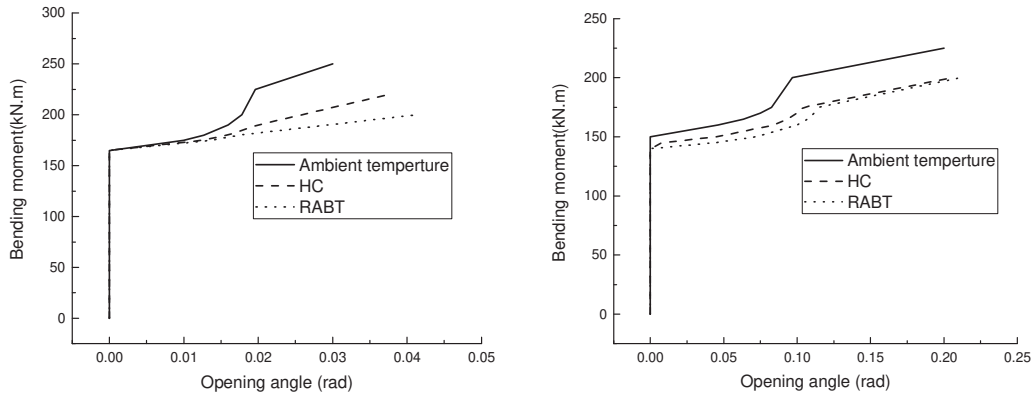

Fig.19. *M*-θ curves with different heating curves: (a) under sagging moments; (b) under hogging moments

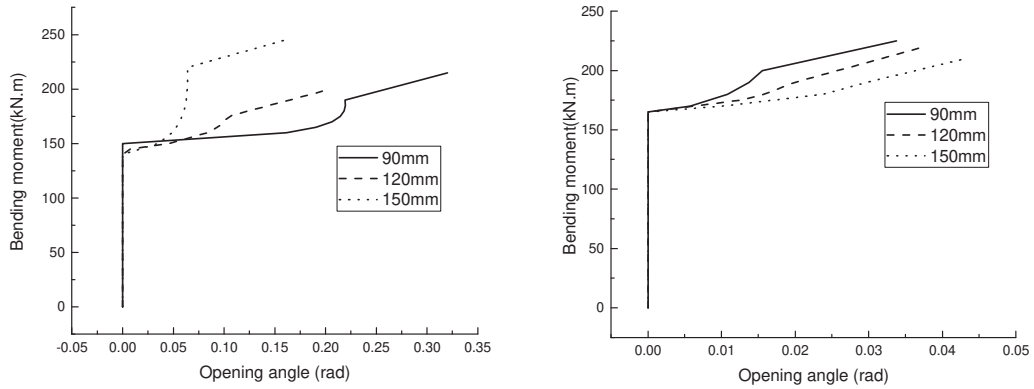

(a) (b)

Fig.20. *M-θ* curves with different bolt locations: (a) under sagging moments; (b) under hogging moments

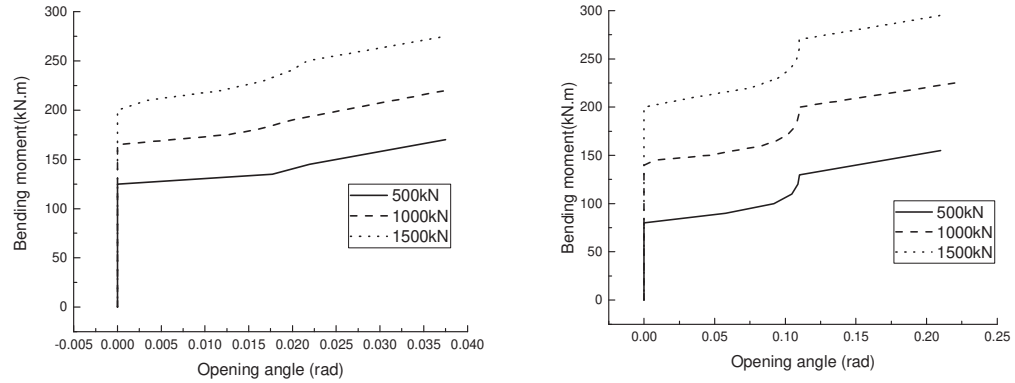

(a) (b)

Fig.21. *M-θ* curves with different initial axial loads: (a) under sagging moments; (b) under hogging moments